RSC Advances

PAPER

View Article Online
View Journal | View Issue

Cite this: *RSC Adv.*, 2024, **14**, 16560

Cool green-emissive $Y_2Si_2O_7$:Tb^{3+} nanophosphor: auto-combustion synthesis and structural and photoluminescence characteristics with good thermal stability for lighting applications†

Pawan Kumar,[a] Devender Singh, *[a] Sonika Kadyan,[a] Harish Kumar[b] and Ramesh Kumar[c]

Received 5th April 2024
Accepted 26th April 2024

DOI: 10.1039/d4ra02571g

rsc.li/rsc-advances

A cheap, versatile, sustainable and energy-efficient gel-combustion method was applied to develop a series of green-emitting down-converted $Y_2Si_2O_7$:Tb^{3+} (YPS:Tb^{3+}) nanophosphors. Employing XRD-based Rietveld refinement approach, the phase purity and crystallographic evaluation of the produced phosphor were conducted, revealing a triclinic crystal with $P\bar{1}$ space group. EDX and TEM analyses were performed on the synthesized samples to determine their elemental composition and morphological properties. Diffuse reflectance spectra yielded 5.61 eV and 5.79 eV optical energy band gaps for the host and the optimized (0.04 mole of Tb^{3+}) sample, respectively. UV light has the ability to excite the nanocrystalline phosphor in an efficient manner, leading to significant luminosity qualities attributed to the radiative relaxation of $^5D_4 \rightarrow {}^7F_J$ (J = 6, 5, 4, 3). The bi-exponential decay function was derived by the PL decay curves. With an activation energy of 0.2206 eV, the $Y_{1.96}Si_2O_7$:$0.04Tb^{3+}$ phosphor exhibits good thermal quenching capabilities. Improved photometric attributes including CIE coordinates, CCT and color purity confirmed the green glow, indicating a strong competitor for cool-green emission in lighting applications.

1 Introduction

Conserving energy is crucial and has great significance for the well-being of future generations as it actively contributes to environmental preservation.[1,2] In recent times, there has been a growing focus on the study of solid-state lighting, predominantly pc-WLEDs. This attention is driven by the need to raise awareness about energy consumption, conservation efforts, and the associated environmental challenges.[3,4] WLEDs exhibit significant advantages in this context owing to their impressive features including high energy-efficacy, small power consumption, absence of mercury, extended lifespan, compact design, ecological friendliness, and superior illumination compared to conventional fluorescent lamps.[5–8] In the present day, WLEDs have found extensive applications across diverse fields including optical waveguides, backlighting, sensors, automobile headlights, flashlights, solid-state lasers, and common lighting.[9–13] Generally, commercial wLEDs are typically produced by coalescing blue-emanating InGaN-chips with yellow-emitting $Y_3Al_5O_{12}$:Ce^{3+} nanophosphors.[14,15] However, these WLEDs often lack a red module in the visible range, resulting in a white emission with a subpar color-rendering-index and high correlated-color-temperature.[16] To address this issue, an alternative approach involves coating primary red, green, and blue nanophosphors onto a NUV-LED chip, aiming to achieve WLEDs with high rendering-index, proper CCT and adjustable color characteristics.[17–19]

Few studies have been conducted on yttrium orthosilicates (YSO) and for a long time, the focus of research on the luminous characteristics of RE-activated yttrium silicates was only on yttrium pyrosilicates (YPS). The magnetic and electrical characteristics of binary disilicates, particularly those of rare earth disilicates, have been thoroughly studied.[20] Specifically, on activation with RE elements, these materials show optimal performance for luminous applications such as plasma displays, laser materials, and high energy nanophosphors.[21] These phosphors provide very efficient luminescence when excited by UV and cathode rays. Because of their chemical stability, yttrium disilicates, also known as yttrium pyrosilicates ($Y_2Si_2O_7$), are among the most suitable silicates.[22] The photoluminescence of Ce^{3+} and Eu^{3+} was particularly explored with respect to the luminescence characteristics of rare earth-doped

[a]Department of Chemistry, Maharshi Dayanand University, Rohtak-124001, Haryana, India. E-mail: devjakhar@gmail.com

[b]Department of Chemistry, School of Chemical Sciences, Central University of Haryana, Mahendergarh-123031, India

[c]Department of Chemistry, Kurukshetra University, Kurukshetra-136119, Haryana, India

† Electronic supplementary information (ESI) available. See DOI: https://doi.org/10.1039/d4ra02571g

$Y_2Si_2O_7$. Nowadays, the green phosphor is quite popular in the lighting industry. As a result, interest in an effective new green phosphor has grown. The green color-emitter trivalent terbium (Tb^{3+}) is one of the rare earth ions that are most frequently employed as an active center. Its many emission peaks encompass a broad wavelength range from blue to orange light. The ground state spectrum characteristics of the Tb^{3+} ion are ^7F_j (j = 0–6), while its outermost electron arrangement is $4f^8$. The $^5D_4 \rightarrow {}^7F_j$ (j = 0–6) transitions are often the source of the distinctive green emission of Tb^{3+} ions, while the concurrently existing $^5D_3 \rightarrow {}^7F_j$ transitions that produce blue or ultraviolet light are also conceivable.[23,24] Moreover, the luminescence of 4f-electrons is mainly a characteristic inherent to the RE ions and remains unaffected by the crystal field surrounding the luminescent center. This is because the 4f-electrons within the inner layer of Tb^{3+} are protected by the outer electrons of $5s^25p^6$. Consequently, it is believed that Tb^{3+}-activated phosphors would show outstanding stability for the particular emission. This work presents a thorough exploration of the structural and optical features of Tb^{3+}-doped $Y_2Si_2O_7$ (YPS) phosphor that is produced using the gel-combustion process. X-ray diffraction, transmission electron microscopy, energy dispersive X-ray spectroscopy, diffuse reflectance spectroscopy and photoluminescence spectroscopy were employed to comprehensively examine the structural, morphological, and spectroscopic aspects of the prepared series of $Y_{2-x}Si_2O_7{:}xTb^{3+}$ (x = 0.01–0.06 mole) samples to ascertain the suitability of the prepared phosphors in pc-WLEDs.

2 Experimental

2.1 Synthesis and characterization

Employing ecologically-sound gel-combustion synthesis, triclinic symmetry type $Y_{2-x}Si_2O_7{:}xTb^{3+}$ phosphors with variable dopant ion content as x = 0.01–0.06 mole were developed, yielding a product that exhibits excellent crystallinity and homogeneity (Fig. 1). For the implementation of this procedure, precise amounts of [$Y(NO_3)_3{\cdot}6H_2O$], [$Tb(NO_3)_3{\cdot}6H_2O$], silica (SiO_2), urea and nitric acid (HNO_3) were employed. The goal is to maintain a metal nitrate-to-fuel ratio of nearly one. Subsequently, the beaker containing the previously prepared mixture was placed on a hot plate adjusted to 80 °C and warmed for 20 minutes. This step is crucial to ensure the effective infiltration of activator ions (Tb^{3+}) into the $Y_2Si_2O_7$ matrix. Following that, the uniform mixture is initially warmed and subsequently transferred to a muffle furnace preheated to 600 °C for a duration of 15 minutes. During this process, a self-restricted exothermic reaction occurs, resulting in the release of combustible gases (CO_2 and N_2).[25,26] This reaction contributes to the formation of a fluffy powder. Subsequently, the obtained powders were finely grounded, after which they were transferred to an alumina crucible for sintering at 1100 °C for 3 hours. To evaluate the phase purity of the produced phosphors, X-ray diffraction examination was performed using a Rigaku Ultima X-ray diffractometer running at 40 kV and 40 mA with Cu-Kα radiation. Using $BaSO_4$ as the reference standard, an integrated sphere-mounted UV-Vis-NIR spectrophotometer (UV-3600, SHIMADZU) was used to produce the diffuse reflection spectra. Using a transmission electron microscope (JEOL JEM-1400 Plus) running at 120 kV, the morphology of the doped nanopowders was examined. A Hitachi SU-8010 SERIES device was used to carry out the energy dispersive X-ray analysis. Additionally, using a Fluorolog-3-Horiba spectrophotometer fitted with a 150 W xenon lamp, the material's emission and excitation spectra were obtained.

3 Results and discussion

3.1 XRD evaluation

XRD is an approach employed for the structural assessment of the produced phosphors. The resulting XRD patterns for the undoped and $Y_{2-x}Si_2O_7{:}xTb^{3+}$ (x = 0.01–0.06 mole) phosphors

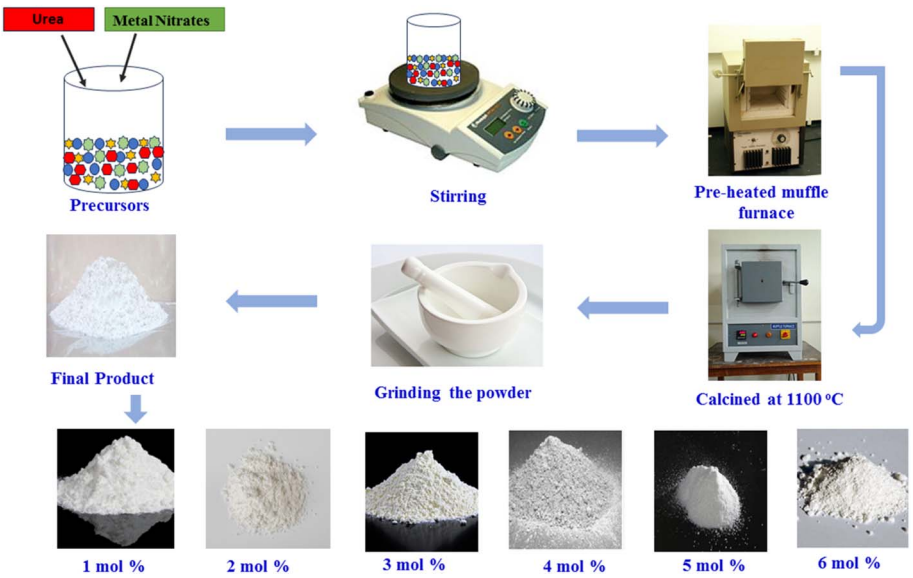

Fig. 1 Synthesis diagram of the gel-combustion process.

are depicted in Fig. 2(a). It was found that the comparable intensity of Tb^{3+}-triggered phosphors and undoped phosphors is essentially indistinguishable. The XRD lines of the $Y_2Si_2O_7$ and $Y_{2-x}Si_2O_7$:xTb^{3+} (x = 0.01–0.06 mole) phosphors were verified *via* the standard JCPDS card [38-0223], which followed the standard pattern of the $Y_2Si_2O_7$ (YPS) material with triclinic phase and $P\bar{1}$ space group.[27,28] It is conceivable to conclude the emergence of single-phase crystal structure since there are no diffraction peaks from the dopant or other phases. XRD patterns remain essentially the same, but a little shift in the diffractions lines toward lower angles, as seen in Fig. 2(b), suggests a propensity for the lattice to expand as the dopant ion's concentration increases. The interplanar distance (d) increases on doping, as listed in Table 1. In order to keep $n\lambda$ constant in Bragg hypothesis ($2d\sin\theta = n\lambda$), the angle (θ) determining their left shift in this case would have to be smaller.[29] The reliable doping of dopant ions in the phosphors may often be assessed by the ion radius resemblance method and the valence state. Another useful technique is to calculate the percentage of variance in the ionic radius of the dopant and the substituted ions. Less than 30% of a percentage difference generally implies the efficient doping of dopant ions.[30] The following eqn (1) may be used to get the percentage difference.[31]

$$D_r = \frac{R_h(CN) - R_d(CN)}{R_h(CN)} \times 100\% \quad (1)$$

In the above relation, R_h(CN) & R_d(CN) stand for the host and entering cation's respective ionic radii as well as coordination number. The results show that the D_r-value is less than 30%, which suggests that the Tb^{3+} ion has successfully replaced the Y^{3+} ion in the $Y_2Si_2O_7$ host. Scherrer is acknowledged for formulating Scherrer's equation, a foundational method in X-ray crystallography used to calculate the average size of crystalline solid materials. It correlates the size of the crystalline domains to the widening of diffraction peaks noted in the X-ray diffraction patterns. The Scherrer's formula is represented by eqn (2).[32]

Table 1 Interplanar d-spacing values of the host and all Tb^{3+}-doped phosphors[a]

Sample	2θ-Angle	d-Spacing (Å)
$Y_2Si_2O_7$ (YPS)	29.32	3.0437 (±0.0094)
YPS:0.01Tb^{3+}	29.31	3.0447 (±0.0068)
YPS:0.02Tb^{3+}	29.30	3.0458 (±0.0072)
YPS:0.03Tb^{3+}	29.28	3.0477 (±0.0066)
YPS:0.04Tb^{3+}	29.25	3.0508 (±0.0069)
YPS:0.05Tb^{3+}	29.23	3.0528 (±0.0085)
YPS:0.06Tb^{3+}	29.20	3.0559 (±0.0081)

[a] Data in () shows the estimated uncertainties.

$$D_{hkl} = \frac{k\lambda}{\beta(2\theta)\cos\theta} \quad (2)$$

In the above formula, λ, β and k represent the wavelength of X-rays (0.154 nm), full width at half-maxima and Scherrer constant (0.89), respectively. The computed crystallite size for all the prepared samples is summarized in Table 2. The following eqn (3), particularly based on the Williamson–Hall formulation, was implemented to corroborate the crystallite size findings described above.[33]

$$\beta_{hkl}\cos\theta_{hkl} = \frac{K\lambda}{D} + 4\varepsilon\sin\theta_{hkl} \quad (3)$$

This method considers the intricate effects of crystallite size and strain on the XRD peaks. It allows for a clear separation of the effects of strain-induced deformation from those caused by the crystallite size, which facilitates more accurate evaluations

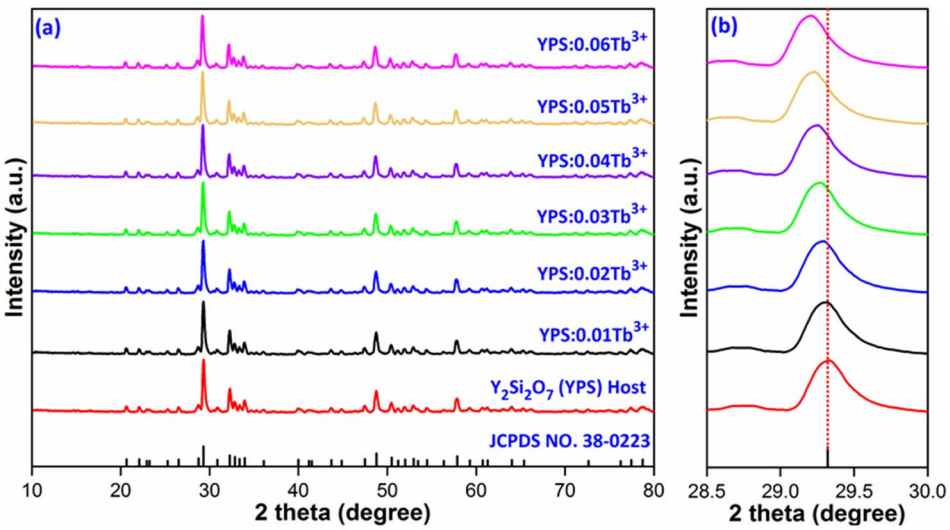

Fig. 2 (a) Diffraction patterns of $Y_2Si_2O_7$ and $Y_{2-x}Si_2O_7$:xTb^{3+} (x = 0.01–0.06 mole) phosphors. (b) Enlarged pattern view of all the considered samples.

Table 2 Diffraction results of the $Y_2Si_2O_7$ and $Y_{2-x}Si_2O_7$:xTb^{3+} (x = 0.01–0.06 mole) phosphors[a]

Sample (YPS)	2 theta (2θ)	FWHM	Crystallite size (nm)		Microstrain ($\varepsilon \times 10^{-4}$)
			Scherrer's	W–H	
$Y_2Si_2O_7$ (YPS)	29.32	0.2997 (±0.00451)	27.40 (±0.0431)	35.58 (±0.0746)	5.1421
YPS:0.01Tb^{3+}	29.31	0.3012 (±0.00341)	27.26 (±0.0254)	34.42 (±0.0879)	5.4532
YPS:0.02Tb^{3+}	29.30	0.3032 (±0.00375)	27.09 (±0.0233)	33.97 (±0.0748)	5.8315
YPS:0.03Tb^{3+}	29.28	0.3071 (±0.00377)	26.74 (±0.0371)	33.12 (±0.0852)	6.0345
YPS:0.04Tb^{3+}	29.25	0.3142 (±0.00314)	26.15 (±0.0322)	32.54 (±0.0901)	6.2931
YPS:0.05Tb^{3+}	29.23	0.3188 (±0.00401)	25.76 (±0.0298)	31.77 (±0.0876)	6.6214
YPS:0.06Tb^{3+}	29.20	0.3219 (±0.00372)	25.52 (±0.0286)	31.04 (±0.0699)	6.8891

[a] Data in () shows the estimated uncertainties.

and interpretations of the material properties. Employing linear fitting on the curve plotted between $4\sin\theta$ and $\beta\cos\theta$, as illustrated in Fig. 3, the crystallite size and strain induced in the phosphor can be determined. The intercept of the linear curve provides an insight into the crystallite size, while the slope offers information about the strain present in the material. This analytical method facilitates a straightforward extraction of both the crystallite size and strain parameters from the X-ray diffraction data. The crystal lattice experienced strain as a result of the replacement of Y^{3+} ions with the larger Tb^{3+} ions. This strain may have limited the size of the particles by lowering their total free energy. The obtained results are listed in Table 2.

A strong method for determining a material's crystal structure from powder X-ray diffraction data is referred to as Rietveld refinement. Through the process of Rietveld refinement, atomic locations, lattice parameters and other structural features of crystalline materials may be precisely determined by comparing the computed patterns based on a suggested crystal structure with the experimental XRD data. The Rietveld refinement patterns for the host and optimized doped phosphors are displayed in Fig. 4(a) and (b). The chi-squared values and reliability factors being within the acceptable range show that the modified profiles show significant agreement with the original structural model. During the refinement process, it becomes evident that the resulting nanophosphor possesses a triclinic phase with the point group symmetry identified as $P\bar{1}$. The outcomes indicate a favorable alignment between the observed and calculated XRD patterns, as evidenced by parameters such as R_{wp}, R_p and χ^2, which fall within acceptable ranges. The refined results, including the lattice parameters, are compiled in Table 3. The convergence of reliability factors yielded R_{wp} values of 7.59% for YPS and 8.42% for YPS:0.04Tb^{3+}, as well as R_p values of 5.77% for YPS and 6.21% for YPS:0.04Tb^{3+}. These values affirm the rationality and reliability of the obtained

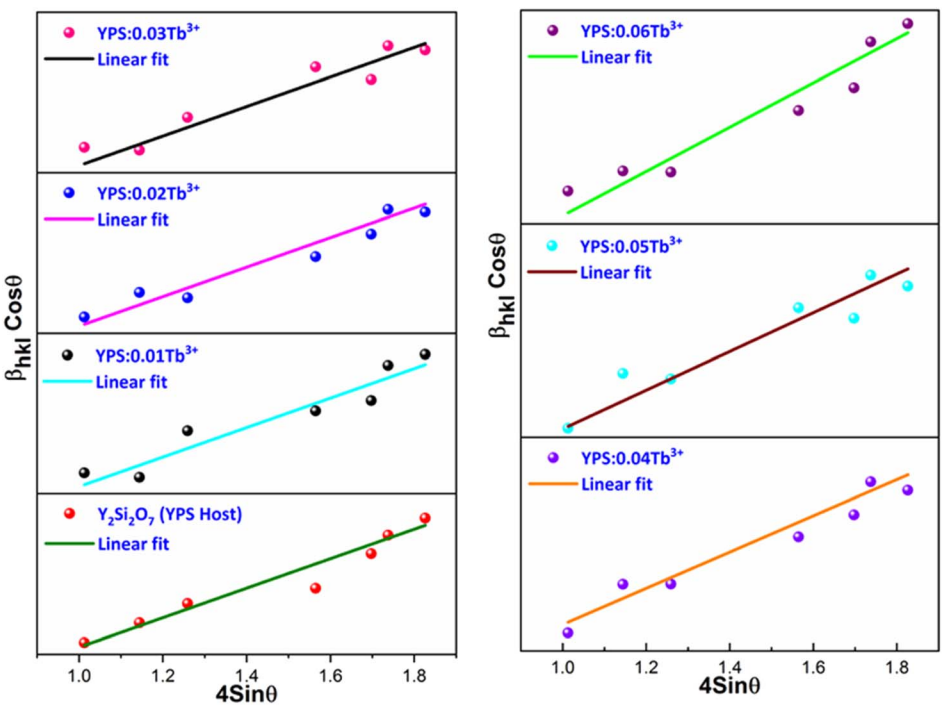

Fig. 3 W–H plot of the $Y_2Si_2O_7$ and various doped $Y_{2-x}Si_2O_7$:xTb^{3+} (x = 0.01–0.06 mole) phosphors.

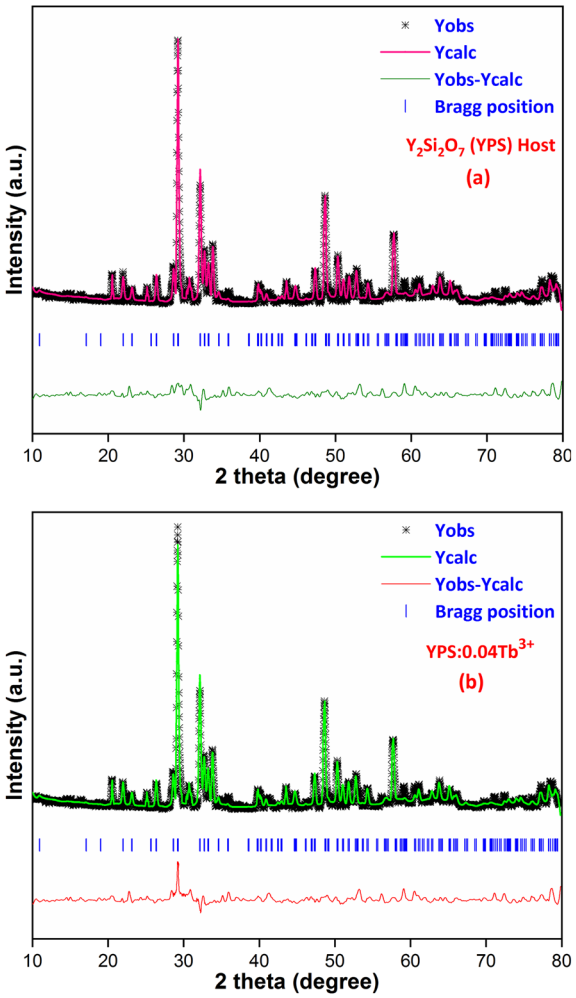

Fig. 4 Rietveld profiles of the (a) $Y_2Si_2O_7$ and (b) $Y_{1.96}Si_2O_7$:0.04Tb^{3+} phosphors.

results. The cell parameters for YPS are indeed smaller than those for the YPS:0.04Tb^{3+} phosphor, as indicated in Table 3. This discrepancy provides additional evidence supporting the successful substitution of Tb^{3+} ions into the Y^{3+} position within the lattice, leading to an expansion of the lattice constants.

3.2 Morphological analysis

The TEM profile presented in Fig. 5 offers valuable insights into the structure of the prepared $Y_{1.96}Si_2O_7$:0.04Tb^{3+} sample. The image vividly illustrates the existence of an aggregated nanocrystalline material characterized by diverse shapes and sizes. The observed aggregation of crystallites is likely attributed to temperature variations experienced during the fabrication process, as suggested by previous studies. Additionally, the porosity evident in the material is linked to the release of gassy by-products through the combustion process.[34,35] This phenomenon contributes to the formation of a porous structure within the material. Notably, the size information obtained from diffraction studies aligns closely with the evaluated size derived from the TEM micrograph. Both analyses indicate

Table 3 Refinement outcomes of the $Y_2Si_2O_7$ (YPS) and YPS:0.04Tb^{3+} phosphors

Sample	$Y_2Si_2O_7$ (YPS)	YPS:0.04Tb^{3+}
2θ range; step (deg.)	10–80; 0.02	10–80; 0.02
System	Triclinic	Triclinic
Lattice-type	P	P
Wavelength (Å)	1.541	1.541
Space group	$P\bar{1}$	$P\bar{1}$
Space group number	2	2
Formula unit (Z)	4	4
α	97.23	97.41
β	89.80	89.83
γ	87.50	87.92
a (Å)	6.556	6.591
b (Å)	6.759	6.781
c (Å)	12.274	12.619
Volume (Å^3)	539.03	558.89
χ^2	3.14	3.97
R_p (%)	5.77	6.21
R_{wp} (%)	7.59	8.42

a nanocrystalline range, specifically within the dimensions of 20–40 nm. This congruence between the XRD and TEM results reinforces the reliability of the characterization, affirming the nanocrystalline nature of the $Y_2Si_2O_7$:Tb^{3+} sample.

3.3 EDX investigation

When a high energy electron beam strikes a sample, it induces the emission of characteristic X-rays from the elements present in the sample. The energy of these X-rays is characteristic of the elements, allowing for the identification and quantification of the elemental composition. The EDX plots of the host $Y_2Si_2O_7$ (YPS) and 0.04 mole-doped YPS nanophosphor are shown in Fig. 6(a) and (b). Numerous peaks that are associated with different elements (Y, Si and O) integrated with the host YPS framework can be seen in the spectrum in Fig. 6(a). The peaks in Fig. 6(b) correspond to Y, Si, O and Tb, further validating the produced phosphor's chemical compositions. The Tb characteristic peaks demonstrate the homogeneous doping of ions in the host matrix. The elemental compositions of the doped sample and the host are shown in the table present in the inset of Fig. 6(a) and (b). The formation of pure $Y_2Si_2O_7$ and

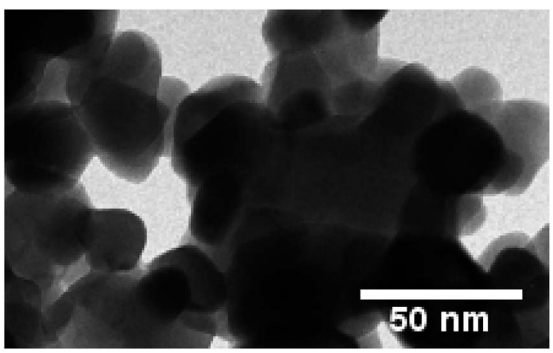

Fig. 5 TEM micrograph of the YPS:0.04Tb^{3+} nanophosphor.

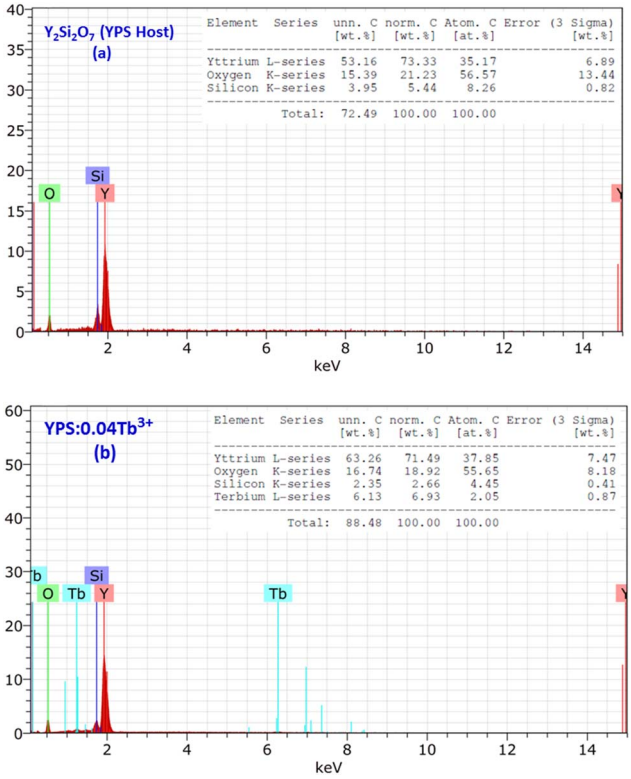

Fig. 6 EDX profiles of the (a) $Y_2Si_2O_7$ and (b) $Y_{1.96}Si_2O_7$:0.04Tb^{3+} phosphors, and the inset represents the chemical composition of the respective samples.

$Y_2Si_2O_7$:Tb^{3+} phosphor is validated by the elements individually, which reflects the findings of XRD.

3.4 Photoluminescence study

3.4.1 Excitation and emission spectra. Fig. 7 illustrates the photoluminescence excitation (PLE) spectrum for $Y_{1.96}Si_2O_7$:0.04Tb^{3+} in the wavelength region of 200–500 nm by fixing the emission at 545 nm. The $4f^8 \rightarrow 4f^75d^1$ transition of Tb^{3+} ions is responsible for the peak that is centered at 258 nm. Additionally, the spectrum disclosed numerous peaks at 301 nm, 325 nm, 347 nm, 367 nm, 386 nm and 489 nm, which originated from the ground state $^7F_6$ and moved to the higher states $^5H_6$, $^5H_7$, $^5L_6$, $^5L_9$, $^5G_6$ and $^5D_4$, respectively.[36,37] To investigate the PL characteristics of $Y_2Si_2O_7$:Tb^{3+} nanophosphors in more detail, the PL emission spectra of powdered YPS:$x$$Tb^{3+}$ (x = 0.01–0.06 mole) nanocrystalline samples were captured at an excitation wavelength of 258 nm, as clearly illustrated in Fig. 8. Numerous emission peaks that correlate to the distinctive Tb^{3+} ion emission in the YPS host matrix can be seen in the spectra. In essence, emission transitions to distinct ^7F_J (J = 2 to 6) energy levels occur from two emission states, $^5D_3$ and $^5D_4$. The $^5D_3$ to $^7F_5$, $^7F_4$ and $^7F_3$ transitions deliver emission peaks at 414 nm, 438 nm and 460 nm, correspondingly. However, four distinct luminous bands of Tb^{3+} ion are characterized and located at about 491 nm ($^5D_4 \rightarrow {}^7F_6$), 544 nm ($^5D_4 \rightarrow {}^7F_5$), 589 nm ($^5D_4 \rightarrow {}^7F_4$) and 624 nm ($^5D_4 \rightarrow {}^7F_3$).[38,39] The

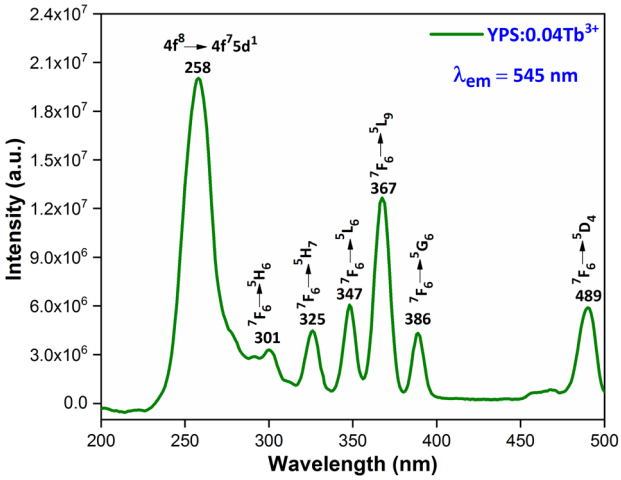

Fig. 7 Excitation spectrum of the $Y_{1.96}Si_2O_7$:0.04Tb^{3+} nanophosphor.

emission peak at 491 nm is the only one that is allowed to be electric-dipole (ED); however, the transitions associated with the other three emission peaks are permitted to be both electric and magnetic-dipole (ED + MD).[40] According to research, the green emission of the YPS:$x$$Tb^{3+}$ (x = 0.01–0.06 mole) nanophosphor is caused by the strongest emission peak that coincides with the $^5D_4 \rightarrow {}^7F_5$ (544 nm) transition. The energy states corresponding to the Tb^{3+} ions in the $Y_2Si_2O_7$ host materials are displayed in Fig. 9.

3.4.2 Concentration quenching (CQ). To determine the most effective doping concentration for Tb^{3+} ions in YPS:$x$$Tb^{3+}$ (0.01–0.06 mole) phosphors, we analyze the variation in the integrated emission intensity with respect to the Tb^{3+} concentration (Fig. 10). The findings indicate that as the doping content increases from 0.01 mole to 0.04 mole, the emission intensity initially increases, reaching its maximum at x = 0.04 mole, and subsequently diminishes. This implies that the optimum amount of Tb^{3+} ions within the YPS host is 0.04 mole,

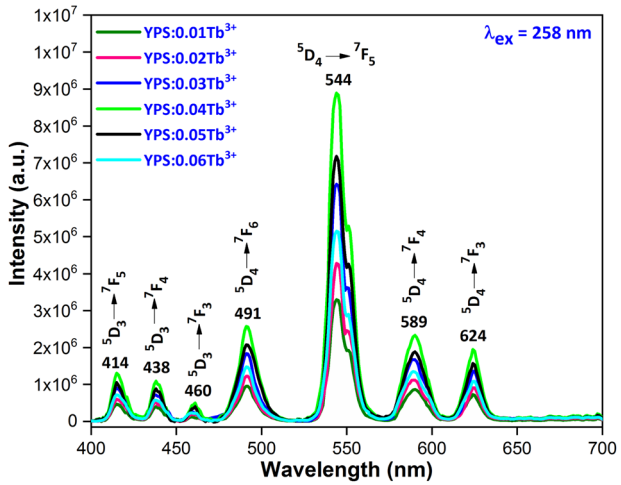

Fig. 8 Emission spectrum of the $Y_{2-x}Si_2O_7$:$x$$Tb^{3+}$ (x = 0.01–0.06 mole) phosphors.

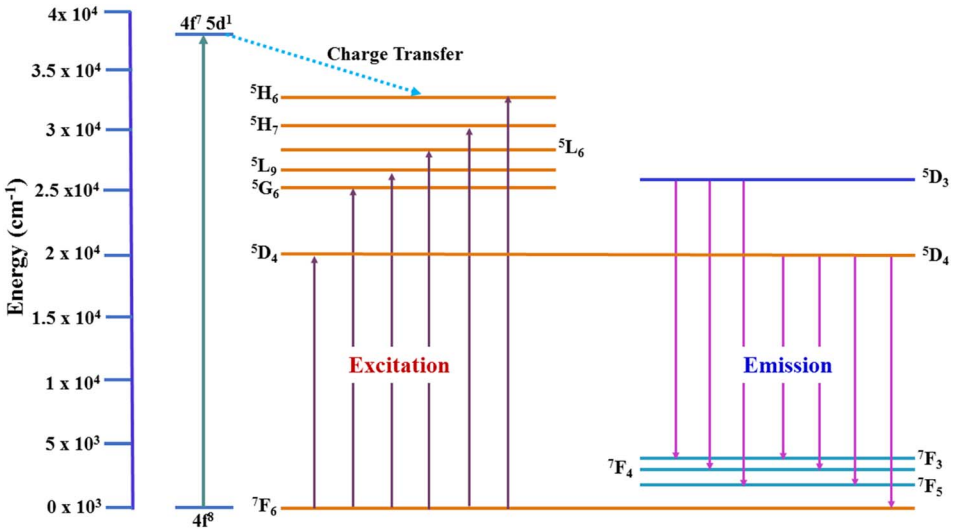

Fig. 9 Energy level diagram for Tb^{3+} ions in the $Y_2Si_2O_7$ nanophosphor.

after which the luminous intensity declines due to concentration quenching. This phenomenon, commonly observed in Tb^{3+} ions-doped inorganic phosphors, is characterized by increased cross-relaxation and energy relocation amid nearby Tb^{3+} ions at higher doping concentrations. Eventually, a portion of the excited energy of Tb^{3+} ions is absorbed by nearby quenching centers, resulting in a decline in the emission intensity. The concentration quenching effect primarily arises from non-radiative energy transfer among Tb^{3+} activators, assisted *via* three pathways: radiation reabsorption, exchange interaction and electric multipolar interaction. Our focus will be on elucidating the mechanism behind CQ in the YPS:Tb^{3+} phosphors. As both exchange interaction and multipolar interaction are influenced by the critical distance (R_c) between Tb^{3+} ions, we analyzed R_c for YPS:Tb^{3+} nanophosphors *via* eqn (4) suggested by Blasse.[41]

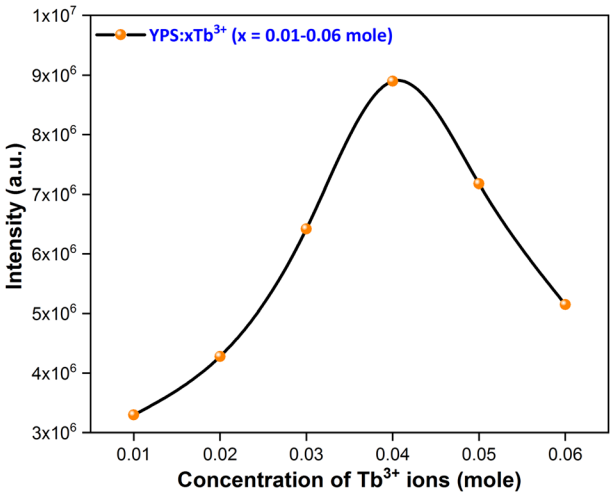

Fig. 10 Concentration quenching profile of the considered nanophosphors.

$$R_c = 2\left(\frac{3V}{4\pi x_c Z}\right)^{1/3} \quad (4)$$

In this context, R_c represents the separation among adjacent Tb^{3+} ions at optimal content, V denotes volume, x_c denotes the optimal amount of dopants and Z signifies cations per unit cell. Given the values $V = 558.89$ Å^3, $x_c = 0.04$ and $Z = 4$, the calculated R_c is approximately 18.828 Å, exceeding the 5 Å threshold. If the critical distance is greater than 5 Å, then multipolar interaction us dominant over exchange interaction. In this scenario, the energy transfer is solely driven by electric multipolar interaction. As the doping amount of terbium ions rises, the distance between Tb^{3+} ions shrinks, thus enhancing the probability of energy transfer between them. The relationship between $\log(I/x)$ and $\log(x)$ for YPS:Tb^{3+} nanophosphors was evaluated using eqn (5) below.[42]

$$\mathrm{Log}\left(\frac{I}{x}\right) = k - \frac{M}{3}\log(x) \quad (5)$$

In above equation, x represents the doping concentration of Tb^{3+} ions, I signifies the PL intensity of samples, and M denotes the electric multipole index. The values of M such as $M = 6$, 8 and 10 correspond to dipole–dipole, dipole–quadrupole and quadrupole–quadrupole interactions, respectively.[43,44] In Fig. 11, the graph between $\log(I/x)$ and $\log(x)$ is depicted, and the slope of the fitted line is determined to be −2.28. Consequently, the calculated value of M is 6.48, agreeing closely with the value of 6. Hence, the dipole–dipole interaction is identified as the primary reason responsible for the CQ effect in the $Y_2Si_2O_7$:Tb^{3+} phosphors.

3.5 Luminescence lifetime

The decay curves for the $^5D_4$ level were recorded at room temperature, employing 258 nm excitation for the

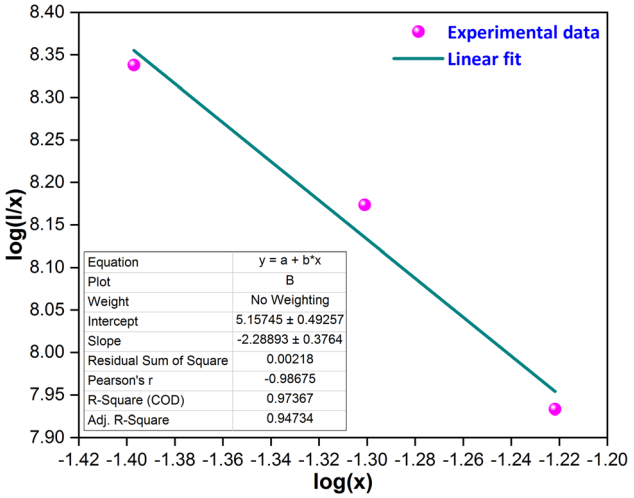

Fig. 11 Straight line fitted graph between log(*x*) and log(*I*/*x*).

$Y_{1.96}Si_2O_7$:0.04Tb^{3+} phosphor, as illustrated in Fig. 12. Also, the inset of Fig. 12 contains the log-based lifetime graph for the considered sample. The experimental decay curve data were fitted using various exponential equations, and the most optimal fit was achieved with the bi-exponential eqn (6).[45]

$$I_t = I_0 + A_1 \exp(-t/\tau_1) + A_2 \exp(-t/\tau_2) \quad (6)$$

here, I_t and I_0 denote luminescence intensities at time t and 0, respectively. τ_1 and τ_2 correspond to the values of the lifetime for the fast and slow exponential components, respectively. Additionally, A_1 and A_2 are constants associated with the parameters for curve fitting. Formula (7) was used to determine the average lifetime for the fabricated phosphors.[46]

$$\tau_{avg} = (A_1 t_1^2 + A_2 t_2^2)/(A_1 t_1 + A_2 t_2) \quad (7)$$

Table 4 displays the average decay lifetimes (τ_{avg}) for all the synthesized doped samples. Notably, it is evident that the decay

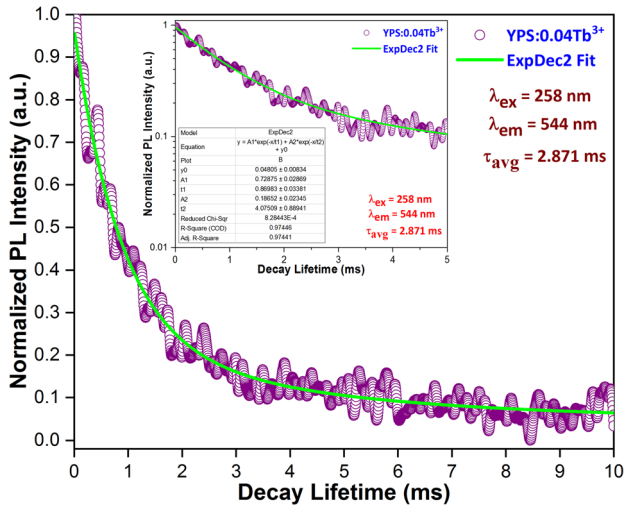

Fig. 12 Lifetime curve of the $Y_{1.96}Si_2O_7$:0.04Tb^{3+} nanophosphor.

times exhibit a decrease with an increase in the doping amount of the trivalent terbium ion. This phenomenon can be attributed to the increasing concentration of dopant ions, causing them to be in closer proximity. Consequently, there is a swift transfer of energy between ions, leading to different decay paths and ultimately resulting in a reduced decay lifetime. Fig. 13 further illustrates that the τ_o value was found to be 4.339 ms, as determined through Auzel's fitting using eqn (8).[47]

$$1\tau_C = \tau_0 \Big/ \left(1 + \frac{C}{C_0} e^{(-N/3)}\right) \quad (8)$$

The quantum efficacy (η) of the produced materials was assessed by the ratio of experimental lifetime (τ_{avg}) to radiative lifetime value (τ_o), as given by eqn (9) below.[48]

$$\eta = \tau_{avg}/\tau_0 \quad (9)$$

The following formula (10) was employed to calculate the non-radiative transition rate (A_{nR}) with the help of the experimental and radiative lifetime values.

$$\frac{1}{\tau_{avg}} = \frac{1}{\tau_0} + A_{nR} \quad (10)$$

Table 4 contains the calculated values of lifetime, quantum efficiency and non-radiative transitions for all the synthesized YPS:$x$$Tb^{3+}$ (x = 0.01–0.06 mole) nanophosphors.

3.6 Optical band gap analysis

Fig. 14 illustrates the characteristic diffuse reflectance spectra (DRS) of both the host and the YPS:0.04Tb^{3+} nanophosphor in the 200–600 nm range. The doped sample exhibits an absorption band at 258 nm, corresponding to the f–d transition of Tb^{3+} ions. Additionally, the absorption peaks attributed to the f–f transitions of Tb^{3+} are observed in the longer wavelength spectral region, specifically at 325 nm ($^7F_6 \rightarrow {}^5H_7$), 367 nm ($^7F_6 \rightarrow {}^5L_9$) and 487 nm ($^7F_6 \rightarrow {}^5D_4$). To explore the impact of Tb^{3+} doping on the band gap (E_g) of the YPS host, the sample's acquired DRS data were transformed into optical absorption data employing the Kubelka–Munk formula illustrated in eqn (11).[49]

$$F(R) = \frac{K}{S} = \frac{(1-R)^2}{2R} \quad (11)$$

Table 4 Decay time and quantum efficiency of the $Y_{2-x}Si_2O_7$:$x$$Tb^{3+}$ (x = 0.01–0.06 mole) phosphors[a]

Sample	τ_{avg} (ms)	A_{nR} (S^{-1})	(η%)
YPS:0.01Tb^{3+}	3.73 (±0.014)	37.69	85.96
YPS:0.02Tb^{3+}	3.49 (±0.015)	56.13	80.43
YPS:0.03Tb^{3+}	3.17 (±0.012)	85.05	73.06
YPS:0.04Tb^{3+}	2.87 (±0.017)	118.03	66.14
YPS:0.05Tb^{3+}	2.52 (±0.013)	166.42	58.07
YPS:0.06Tb^{3+}	2.29 (±0.015)	206.28	52.77

[a] Data in () shows the estimated uncertainties.

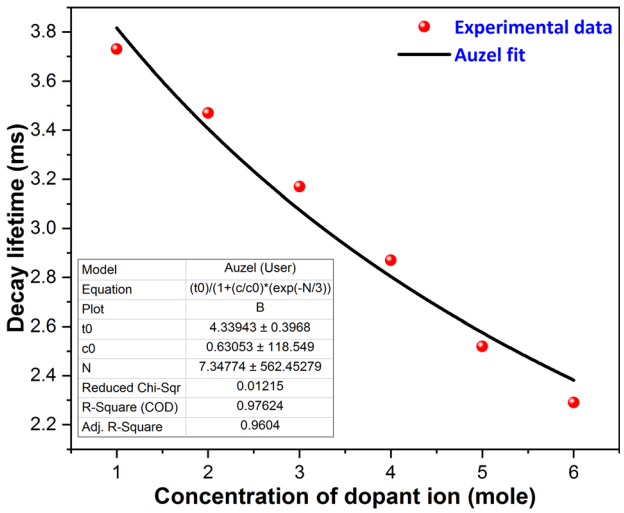

Fig. 13 Auzel's fitting curve of the $Y_{2-x}Si_2O_7$:xTb^{3+} (x = 0.01–0.06 mole) phosphors.

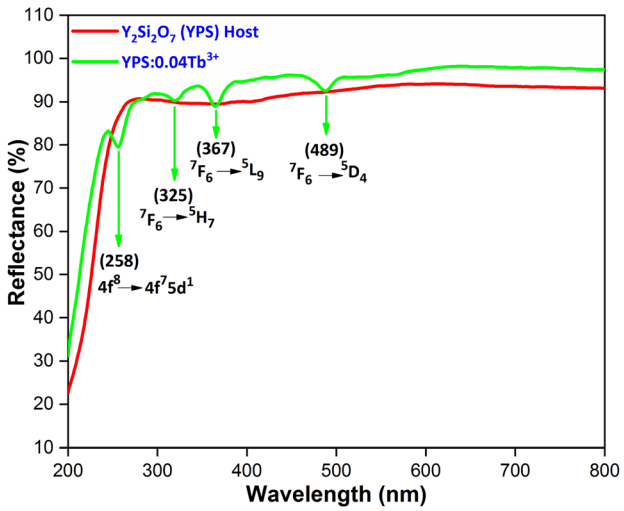

Fig. 14 Diffusion reflectance spectra of the host and $Y_{1.96}Si_2O_7$:0.04Tb^{3+} nanophosphor.

The symbols for the reflection coefficient, scattering coefficient, and molar absorption coefficient are K, S, and R, respectively. Eqn (12) explains the relationship between E_g and the absorption coefficient (α) using Tauc's formula.

$$\alpha = \frac{C_1(h\nu - E_g)^{1/2}}{h\nu} \quad (12)$$

Band gap energy will be conceivable from eqn (11) and (12), which utilised formula (13).[50]

$$[F(R)h\nu] = C_2(h\nu - E_g)^{1/2} \quad (13)$$

The band gap (E_g) of the sample is indicated by extrapolating the resulting curve to the $h\nu$ axis (x-axis), where $[F(R)h\nu]^2 = 0$. This is achieved through a plot of $[F(R)h\nu]^2$ *versus* $h\nu$, as illustrated in Fig. 15. The band gaps for the host YPS and YPS:0.04Tb^{3+} phosphor are 5.61 eV and 5.79 eV, respectively. Burstein–Moss (B–M) theory results in a continual rise of the optical energy gap from the host to the doped sample.

3.7 Temperature-dependent luminescence

The thermal stability of a phosphor at elevated temperatures is a crucial factor in applications involving solid-state lighting. The temperature-dependent photoluminescence spectra of the YPS:0.04Tb^{3+} phosphor were examined across a range of temperatures from 298 to 498 K, as illustrated in Fig. 16. The peak's shapes and locations in the spectra remained consistent as the temperature rose. A gradual reduction in intensity has been attributed to an increased occurrence of non-radiative transitions. To evaluate the impact of thermal quenching, the activation energy may be determined by Arrhenius eqn (14).[51,52]

$$I_T = \frac{I_0}{1 + A\exp\left(-\frac{E_a}{kT}\right)} \quad (14)$$

Eqn (14) is further modified as

$$\mathrm{Ln}\left(\frac{I_0}{I_T} - 1\right) = \ln A - \frac{E_a}{kT} \quad (15)$$

here, E_a, k, I_T and I_0 stand for activation energy, Boltzmann constant, intensity at temperature T and original intensity, respectively. As depicted in Fig. 17, a linear relationship is observed between $\ln[(I_0/I_T) - 1]$ and $1/kT$ for the YPS:0.04Tb^{3+} phosphor. In accordance with eqn (15), the experimental data fits well with a linear trend, allowing the calculation of the activation energy (E_a) for thermal quenching from the slope. The determined E_a value for thermal quenching is 0.2206 eV, which is further supported by recent literature, *i.e.*, $Ca_2LuHf_2Al_3O_{12}$:Ce^{3+}, Tb^{3+},[53] $Ca_2YHf_2Al_3O_{12}$:Ce^{3+},Tb^{3+},[54] $Ca_{14}Al_{10}Zn_6O_{35}$:Tb^{3+},[55] $Ba_3YB_3O_9$:Tb^{3+},[56] $RbBaBP_2O_8$:Tb^{3+},[57] $Ca_2Ga_2SiO_7$:Tb^{3+},[58] La_4GeO_8:Tb^{3+}, Eu^{3+},[59] $Ba_3(ZnB_5O_{10})$

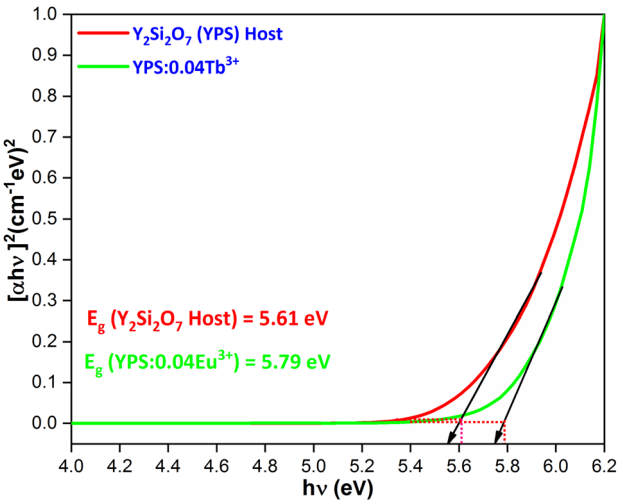

Fig. 15 Tauc's plot for the $Y_2Si_2O_7$ and $Y_{1.96}Si_2O_7$:0.04Tb^{3+} phosphor.

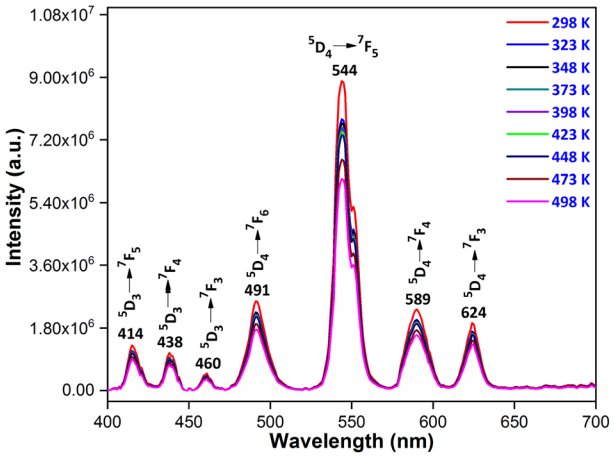

Fig. 16 Temperature-dependent photoluminescence of the $Y_{1.96}Si_2O_7$:0.04Tb^{3+} phosphor.

PO_4:Tb^{3+},[60] Bi_3TeBO_9:Tb^{3+}[61] and $Na_5Lu_9F_{32}$:Tb^{3+}.[62] In the present study, multiphonon-assisted nonradiative transition did not occur. The multiphonon-assisted nonradiative transition process is a mechanism that can contribute to quenching luminescence in rare-earth-doped materials. The multiphonon-assisted nonradiative transition typically occurs when there is a small energy gap between the excited state and lower-lying states. This energy gap might be relatively larger in $Y_2Si_2O_7$ doped with Tb^{3+} ions, reducing the likelihood of multiphonon-assisted nonradiative transitions. There may be other nonradiative processes or quenching mechanisms more dominant in this system, such as cross-relaxation or energy transfer to defects. This outcome further suggests that the YPS:0.04Tb^{3+} phosphor exhibits admirable thermal stability for white light-emitting diodes.

3.8 Photometric investigation

The substance that emits light is called a phosphor and the kind of activator regulates the color that the phosphor emits.

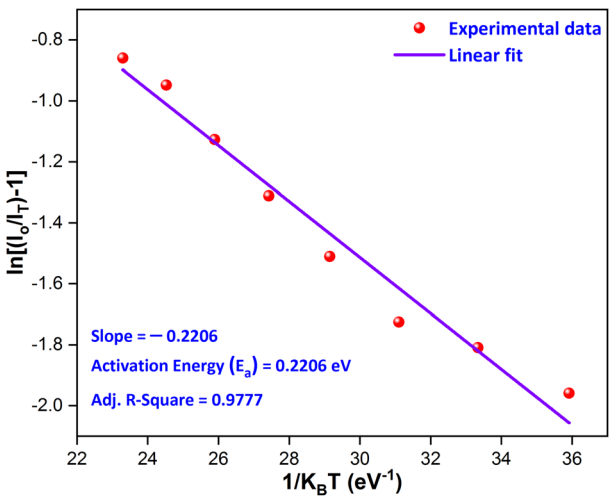

Fig. 17 Linear fitted graph for the calculation of the activation energy.

Assessing the material's photometric behavior is imperative. $\bar{x}(\lambda)$, $\bar{y}(\lambda)$ and $\bar{z}(\lambda)$ are the color matching variables that are employed for assessing the color of the illumination. The values (X, Y and Z), representing the necessary stimulation levels to replicate a color from the spectral intensity, are provided by the eqn (16)–(18) below, where $P(\lambda)$ represents the spectral power distribution of light.[63]

$$X = \int \bar{x}(\lambda)P(\lambda)\mathrm{d}\lambda \quad (16)$$

$$Y = \int \bar{y}(\lambda)P(\lambda)\mathrm{d}\lambda \quad (17)$$

$$Z = \int \bar{z}(\lambda)P(\lambda)\mathrm{d}\lambda \quad (18)$$

The relative fraction of tristimulus values, or chromaticity coordinates, can be obtained *via* the resulting formula (19).

$$x = \frac{X}{X+Y+Z} \text{ and } y = \frac{Y}{X+Y+Z} \quad (19)$$

The CIE coordinates of the YPS:$x$$Tb^{3+}$ (x = 0.01–0.06 mole) phosphors are located in the green area of the color gamut, as revealed in Fig. S1–S6.† The color purity (CP) in context of the nanophosphors typically refers to the ability of the nanophosphors to emit light of a specific color without any undesired spectral impurities or broadening. The color purity of the achieved phosphors was evaluated using the given formula (20).[64,65]

$$\mathrm{CP} = \sqrt{\frac{(x-x_i)^2+(y-y_i)^2}{(x_d-x_i)^2+(y_d-y_i)^2}} \times 100 \quad (20)$$

The CCTs in Kelvin (K) indicate the color advent of light output through an illumination source. Whether a light source appears warm or cool may be determined by examining its CCT. Cool white light is indicated by a CCT above 4000 K, whereas warm light is signified by a CCT below 3000 K. To calculate the CCT values, CIE points representing the light source were renewed to (u', v') by eqn (21) below. The subsequent step involved defining the temperature associated with the Planckian locus closest to the light source on the (u', v') uniform chromaticity chart portrayed in Fig. S7–S12.† This process allows for the identification of the temperature on the Planckian locus that is in proximity to the given light source's coordinates on the chromaticity diagram.[66]

$$u' = \frac{4x}{-2x+12y+3}, \quad v' = \frac{9y}{-2x+12y+3} \quad (21)$$

Additionally, McCamy's third-order polynomial was utilized for computing the CCT values based on the Kelvin (K) scale to assess the quality of light, given by eqn (22).[67]

$$\mathrm{CCT} = -437n^3 + 3601n^2 - 6861n + 5514.31 \quad (22)$$

here, (x, y) are CIE coordinates, $n = (x - x_e)/(y - y_e)$ is the inverse slope line, and x_e and y_e = 0.332 and 0.186 are the values of chromaticity epicenters. The values of photometric variables

Table 5 Chromaticity parameters of the $Y_{2-x}Si_2O_7$:xTb^{3+} (x = 0.01–0.06 mole) phosphors[a]

Sample	(x, y)	CP (%)	(u', v')	CCT (K)
YPS:0.01Tb^{3+}	0.3401, 0.5125 (±0.00011, 0.00012)	56.4 (±0.26)	0.1606, 0.5446 (±0.00013, 0.00014)	5346.37 (±6.14)
YPS:0.02Tb^{3+}	0.3422, 0.5069 (±0.00013, 0.00011)	55.3 (±0.21)	0.1630, 0.5432 (±0.00012, 0.00011)	5299.89 (±9.14)
YPS:0.03Tb^{3+}	0.3418, 0.5057 (±0.00013, 0.00010)	54.8 (±0.25)	0.1630, 0.5428 (±0.00014, 0.00016)	5307.39 (±7.34)
YPS:0.04Tb^{3+}	0.3389, 0.5175 (±0.00012, 0.00011)	57.5 (±0.27)	0.1589, 0.5459 (±0.00012, 0.00014)	5373.09 (±4.18)
YPS:0.05Tb^{3+}	0.3412, 0.5181 (±0.00014, 0.00014)	58.4 (±0.24)	0.1599, 0.5463 (±0.00012, 0.00014)	5327.01 (±6.16)
YPS:0.06Tb^{3+}	0.3424, 0.5097 (±0.00015, 0.00012)	56.2 (±0.32)	0.1625, 0.5441 (±0.00014, 0.00013)	5297.57 (±6.18)

[a] Data in () shows the estimated uncertainties.

such as CIE, CP and CCT of all the synthesized $Y_{2-x}Si_2O_7$:xTb^{3+} (x = 0.01–0.06 mole) phosphors are summarized in Table 5.

4 Conclusions

Nanophosphors composed of yttrium disilicates ($Y_2Si_2O_7$) doped with terbium (Tb^{3+}) were produced through a gel-combustion technique. The diffraction patterns of the phosphors indicated a triclinic single-phase structure. Using Scherrer's equation and W–H plot, the crystallite size was determined to be 24–36 nm, and TEM exploration validated this value. The excitation of the phosphors at 258 nm resulted in a vivid green luminescence. The blue region exhibited distinctive luminescence and luminous bands at 417 nm, 436 nm and 458 nm, which are attributed to the $^5D_3 \rightarrow {}^7F_J$ (J = 5, 4, 3) transitions of terbium ions. The peaks in the green region correspond to the $^5D_4 \rightarrow {}^7F_J$ (J = 6, 5, 4, 3) transitions of Tb^{3+} ions, which are caused by the f–f transitions of Tb^{3+} cations in the given lattice and are attributed to dipole–dipole interactions. Based on the emission spectra, the CIE chromaticity coordinates were computed and were found to fall inside the green region. As a result, the current phosphor is very beneficial for lighting applications.

Data availability

Data will be made available on request.

Author contributions

Pawan Kumar: data curation, writing – original draft, investigation, methodology; Devender Singh: writing – review & editing, resources, supervision; Sonika Kadyan: validation; Harish Kumar: software; Ramesh Kumar: visualization.

Conflicts of interest

The authors declare that they have no known competing financial interests or personal relationships that could have appeared to influence the work reported in this paper.

Acknowledgements

Pawan Kumar is thankful to UGC-New Delhi for providing SRF [117/(CSIRNETJUNE2019)]. Devender Singh is grateful to MDU, Rohtak for Post Seed Grant under research promotion scheme.

References

1 R. Naik, S. C. Prashantha, H. Nagabhushana, S. C. Sharma, B. M. Nagabhushana, H. P. Nagaswarupa and H. B. Premkumar, Low temperature synthesis and photoluminescence properties of red emitting Mg_2SiO_4:Eu^{3+} nanophosphor for near UV-light emitting diodes, *Sens. Actuators, B*, 2014, **195**, 140–149, DOI: 10.1016/j.snb.2014.01.018.

2 D. Singh, V. Tanwar, S. Bhagwan and I. Singh, Recent Advancements in Luminescent Materials and Their Potential Applications, *Adv. Magn. Opt. Mater.*, 2016, 317–352, DOI: 10.1002/9781119241966.ch10.

3 V. Singh, S. Kaur and M. Jayasimhadri, Luminescence properties of orange emitting $CaAl_4O_7$:Sm^{3+} phosphor for solid state lighting applications, *Solid State Sci.*, 2020, **101**, 106049, DOI: 10.1016/j.solidstatesciences.2019.106049.

4 I. Gupta, P. Kumar, S. Singh, S. Bhagwan, S. K. Chhikara and D. Singh, Crystal configuration, spectroscopic and optical characteristics of Er^{3+} doped $YAlO_3$ perovskites for advanced photonic appliances, *Inorg. Chim. Acta*, 2022, **543**, 121183, DOI: 10.1016/j.ica.2022.121183.

5 J. Chen, H. Xiang, J. Wang, R. Wang, Y. Li, Q. Shan and H. Zeng, Perovskite white light emitting diodes: progress, challenges, and opportunities, *ACS Nano*, 2021, **15**, 17150–17174, DOI: 10.1021/acsnano.1c06849.

6 D. Singh and S. Sheoran, Synthesis and luminescent characteristics of $M_3Y_2Si_3O_{12}$:Eu^{3+} (M = Ca, Mg, Sr and Ba) nanomaterials for display applications, *J. Mater. Sci.: Mater. Electron.*, 2017, **27**, 12707–12718, DOI: 10.1007/s10854-016-5405-5.

7 I. Gupta, S. Singh, S. Bhagwan and D. Singh, Rare earth (RE) doped phosphors and their emerging applications: a review, *Ceram. Int.*, 2021, **47**, 19282–19303, DOI: 10.1016/j.ceramint.2021.03.308.

8 D. Singh, V. Tanwar, A. P. Simantilleke, S. Bhagwan, B. Mari, P. S. Kadyan and I. Singh, Synthesis and enhanced luminescent characterization of $SrAl_4O_7$:Eu^{2+}, RE^{3+} (RE = Nd, Dy) nanophosphors for light emitting applications, *J. Mater. Sci.: Mater. Electron.*, 2016, **27**, 5303–5308, DOI: 10.1007/s10854-016-4428-2.

9 R. Fouad and M. Saif, Synthesis, spectroscopic and photoluminescence studies of novel Eu^{3+} nanophosphor complex as fluorescent sensor for highly sensitive detection of latent fingerprints and anti-counterfeiting, *J. Mol.*

Struct., 2020, **1217**, 128472, DOI: 10.1016/j.molstruc.2020.128472.

10 P. Kumar, S. Singh, I. Gupta, K. Nehra, V. Kumar and D. Singh, Structural refinement and optical characteristics of single-phase $Gd_3Al_5O_{12}:Er^{3+}$ nanophosphors for luminescent applications, *J. Lumin.*, 2022, **252**, 119338, DOI: 10.1016/j.jlumin.2022.119338.

11 G. L. Bhagyalekshmi and D. N. Rajendran, Luminescence dynamics of Eu^{3+} activated and co-activated defect spinel zinc titanate nanophosphor for applications in WLEDs, *J. Alloys Compd.*, 2021, **850**, 156660, DOI: 10.1016/j.jallcom.2020.156660.

12 P. Kumar, D. Singh, I. Gupta, S. Singh, S. Nehra and R. Kumar, A study of phase evolution, crystallographic and down-conversion luminescent behaviour of monoclinic $Y_4Al_2O_9:Dy^{3+}$ nanophosphors for white light applications, *Opt. Mater.*, 2023, **138**, 113677, DOI: 10.1016/j.optmat.2023.113677.

13 P. Kumar, S. Singh, I. Gupta, V. Kumar and D. Singh, Er^{3+}-activated $LaAlO_3$ perovskite phosphor: crystal structure and down conversion photoluminescent behaviour for optoelectronic devices, *Inorg. Chem. Commun.*, 2022, **1265**, 109578, DOI: 10.1016/j.inoche.2022.109578.

14 V. Tanwar, S. Singh, I. Gupta, P. Kumar, H. Kumar, B. Mari and D. Singh, Preparation and luminescence characterization of Eu (III)-activated Forsterite for optoelectronic applications., *J. Mol. Struct.*, 2022, **1250**, 131802, DOI: 10.1016/j.molstruc.2021.131802.

15 P. Kumar, D. Singh, I. Gupta and H. Kumar, Influence of Dy^{3+} ion concentration on structural, photoluminescence and energy transfer mechanism of promising $GdSr_2AlO_5$ nanophosphors for white light applications, *Ceram. Int.*, 2023, **49**, 29010–29024, DOI: 10.1016/j.ceramint.2023.06.173.

16 X. Yang, Y. Zhang, X. Zhang, J. Chen, H. Huang, D. Wang and B. Lei, Facile synthesis of the desired red phosphor $Li_2Ca_2Mg_2Si_2N_6:Eu^{2+}$ for high CRI white LEDs and plant growth LED device, *J. Am. Ceram. Soc.*, 2020, **103**, 1773–1781, DOI: 10.1111/jace.16858.

17 P. Kumar, S. Singh, I. Gupta, V. Kumar and D. Singh, Luminous $LaAlO_3:Dy^{3+}$ perovskite nanomaterials: synthesis, structural, and luminescence characteristics for white light-emitting diodes, *Luminescence*, 2022, **37**, 1932–1941, DOI: 10.1002/bio.4377.

18 Y. Bai, Z. Jia, J. Gao, L. Wu, Y. Kong, Y. Zhang and J. Xu, A novel red-emitting phosphor $K_2MgGeO_4:Eu^{3+}$ for WLEDs: zero-thermal quenching induced by heterovalent substitution, *J. Mater.*, 2022, **10**, 15957–15966, DOI: 10.1039/D2TC03500F.

19 T. S. Dhapodkar, A. R. Kadam, N. Brahme and S. J. Dhoble, Efficient white light-emitting $Mg_{21}Ca_4Na_4(PO_4)_{18}:Dy^{3+}$, Tb^{3+}, Eu^{3+} triple-doped glasses: a multipurpose glasses for WLEDs, solar cell efficiency enhancement, and smart windows applications, *Mater. Today Chem.*, 2022, **24**, 100938, DOI: 10.1016/j.mtchem.2022.100938.

20 P. Kantuptim, H. Fukushima, H. Kimura, D. Nakauchi, T. Kato, M. Koshimizu and T. Yanagida, VUV-and X-ray-induced properties of $Lu_2Si_2O_7$, $Y_2Si_2O_7$, and $Gd_2Si_2O_7$ single crystals, *Sens. Mater.*, 2021, **33**, 2195, DOI: 10.18494/SAM.2021.3316.

21 X. Xu, Z. Xiao, Y. Wang, Y. Yan, J. Shen, Y. Nie and F. Lai, Structure and upconversion luminescence properties of Pr^{3+}-doped $Y_2Si_2O_7$ phosphor prepared by different methods, *Opt. Mater.*, 2022, **134**, 113191, DOI: 10.1016/j.optmat.2022.113191.

22 S. Liu, H. Cui, M. Liu, J. Chen, M. Wen, S. Li and X. Sun, Spherical red-emitting X1-Y_2SiO_5:Eu and α-$Y_2Si_2O_7$:Eu phosphors with high color purity: the evolution of morphology, phase and photoluminescence upon annealing, *Ceram. Int.*, 2022, **48**, 8641–8652, DOI: 10.1016/j.ceramint.2021.12.075.

23 P. Kumar, S. Singh, I. Gupta, A. Dalal, V. Kumar and D. Singh, Preparation, structural and photometric properties of single-phased $Gd_3Al_5O_{12}:Tb^{3+}$ green-emitting phosphors for solid state lighting purpose, *J. Mater. Sci. Eng. B*, 2023, **288**, 116189, DOI: 10.1016/j.mseb.2022.116189.

24 H. Tang, D. Yang, H. Li, M. Li and J. Zhu, A narrow-band $RbBaBP_2O_8$: Tb^{3+} green phosphor with high thermal stability for backlighting display application, *J. Lumin.*, 2023, **257**, 119733, DOI: 10.1016/j.jlumin.2023.119733.

25 I. Gupta, S. Singh, P. Kumar, S. Bhagwan, V. Kumar and D. Singh, Structural, morphological and optoelectronic aspects of $YAlO_3:Dy^{3+}$ doped nanocrystalline materials for NUV energized WLEDs, *Curr. Appl. Phys.*, 2022, **43**, 78–89, DOI: 10.1016/j.cap.2022.08.011.

26 P. Kumar, D. Singh and H. Kumar, Red-emitting Eu^{3+} activated $LaSr_2AlO_5$ phosphor for wLEDs: crystal structure, photoluminescence, thermal stability, Judd-Ofelt calculation and band-gap analyses, *Mater. Res. Bull.*, 2024, **173**, 112683, DOI: 10.1016/j.materresbull.2024.112683.

27 V. Kahlenberg, W. Wertl, D. M. Többens, R. Kaindl, P. Schuster and H. Schottenberger, Rietveld analysis and Raman spectroscopic investigations on α-$Y_2Si_2O_7$, *Z. Anorg. Allg. Chem.*, 2008, **634**, 1166–1172, DOI: 10.1002/zaac.200700548.

28 J. Sokolnicki, Upconversion luminescence from Er^{3+} in nanocrystalline $Y_2Si_2O_7:Er^{3+}$ and $Y_2Si_2O_7$: Yb^{3+}, Er^{3+} phosphors, *Mater. Chem. Phys.*, 2011, **131**, 306–312, DOI: 10.1016/j.matchemphys.2011.09.046.

29 P. Kumar, S. Singh, I. Gupta, A. Hooda, V. Kumar and D. Singh, Reddish-orange color tunable Sm^{3+} activated $Gd_3Al_5O_{12}$ phosphors: crystallographic and photophysical investigation for lighting applications, *J. Mol. Struct.*, 2023, **1271**, 134074, DOI: 10.1016/j.molstruc.2022.134074.

30 I. Gupta, P. Kumar, S. Singh, S. Bhagwan, S. K. Chhikara and D. Singh, Crystal configuration, spectroscopic and optical characteristics of Er^{3+} doped $YAlO_3$ perovskites for advanced photonic appliances, *Inorg. Chim. Acta*, 2022, **543**, 121183, DOI: 10.1016/j.ica.2022.121183.

31 N. Huang, G. Lu, B. Bai, H. Zhao, W. Yao, C. Cao and A. Xie, Preparation, crystal structure, and photoluminescence properties of Tb^{3+} activated $Lu_2(MoO_4)_3$ green-emitting phosphors, *J. Lumin.*, 2024, **269**, 120475, DOI: 10.1016/j.jlumin.2024.120475.

32 F. T. L. Muniz, M. R. Miranda, C. Morilla dos Santos and J. M. Sasaki, The Scherrer equation and the dynamical theory of X-ray diffraction, *Acta Crystallogr., Sect. A: Found. Adv.*, 2016, **72**, 385–390, DOI: 10.1107/S205327331600365X.

33 P. Kumar, S. Singh, I. Gupta, V. Kumar and D. Singh, Structural and optical characterization of trivalent samarium-activated $LaAlO_3$ nanocrystalline materials for solid-state lighting, *J. Mol. Struct.*, 2022, **1265**, 133362, DOI: 10.1016/j.molstruc.2022.133362.

34 C. Zuo, S. Yang, Z. Cao, H. Yu and X. Wei, Excellent energy storage and hardness performance of $Sr_{0.7}Bi_{0.2}TiO_3$ ceramics fabricated by solution combustion-synthesized nanopowders, *Chem. Eng. J.*, 2022, **442**, 136330, DOI: 10.1016/j.cej.2022.136330.

35 I. Gupta, D. Singh, P. Kumar, S. Singh, S. Bhagwan and V. Kumar, Crystallographic and luminescence studies of $Gd_2Si_2O_7$:Er^{3+} nanomaterials for NUV energized lighting applications, *J. Mol. Struct.*, 2023, **1287**, 135595, DOI: 10.1016/j.molstruc.2023.135595.

36 D. Navami, G. P. Darshan, D. R. Lavanya, H. B. Premkumar, S. C. Sharma, H. Adarsha and H. Nagabhushana, Design of green emitting $CaZrO_3$:Tb^{3+} nanophosphor: luminescence based platform for real-time ultrasensitive detection of latent fingerprints and anti-counterfeiting applications, *Opt. Mater.*, 2021, **122**, 111474, DOI: 10.1016/j.optmat.2021.111474.

37 I. Gupta, D. Singh, S. Singh, P. Kumar, S. Bhagwan and V. Kumar, Phase recognition and spectroscopic characteristics of single-phase Tb^{3+} doped $Gd_4Al_2O_9$ nanophosphors for NUV energized advanced photonic appliances, *J. Lumin.*, 2022, **252**, 119327, DOI: 10.1016/j.jlumin.2022.119327.

38 P. Kumar, D. Singh, I. Gupta, S. Singh, S. Nehra and R. Kumar, Combustion derived single phase $Y_4Al_2O_9$:Tb^{3+} nanophosphor: crystal chemistry and optical analysis for solid state lighting applications, *RSC Adv.*, 2023, **13**, 7752–7765, DOI: 10.1039/D3RA00735A.

39 I. Gupta, D. Singh, S. Singh, P. Kumar, S. Bhagwan, V. Kumar and S. K. Chhikara, Crystallographic, morphological and photoluminescent investigations of Tb^{3+}-doped $YAlO_3$ perovskites for lighting applications, *Luminescence*, 2023, **38**, 585–599, DOI: 10.1002/bio.4486.

40 P. Kumar, D. Singh and I. Gupta, Physical insights into crystal structure and optical response of green light emitting Tb^{3+} activated $GdSr_2AlO_5$ nanophosphors for optical displays, *Mater. Res. Bull.*, 2023, **167**, 112413, DOI: 10.1016/j.materresbull.2023.112413.

41 U. Berwal, V. Singh and R. Sharma, Structural and optical studies on Dy^{3+} doped $Gd_2Ti_2O_7$ pyrochlore as white light emission, *Ceram. Int.*, 2023, **49**, 8897–8906, DOI: 10.1016/j.ceramint.2022.11.045.

42 N. Hussain, S. Rubab and V. Kumar, Spectroscopic characterizations and investigation of Judd-Ofelt intensity parameters of Dy^{3+} doped $Ba_2La_8(SiO_4)_6O_2$ near white light emitting phosphor, *Ceram. Int.*, 2023, **49**, 15341–15348, DOI: 10.1016/j.ceramint.2023.01.118.

43 P. Kumar, D. Singh, I. Gupta, S. Singh, S. Nehra and R. Kumar, Realization of warm reddish-orange light emitter single phase $Y_4Al_2O_9$:Sm^{3+} nanophosphors for indoor lighting applications, *J. Lumin.*, 2023, **257**, 119703, DOI: 10.1016/j.jlumin.2023.119703.

44 Y. Tian, B. Chen, B. Tian, R. Hua, J. Sun, L. Cheng, H. Zhong, X. Li, J. Zhang, Y. Zheng, T. Yu, L. Huang and Q. Meng, Concentration-dependent luminescence and energy transfer of flower-like $Y_2(MoO_4)_3$:Dy^{3+} phosphor, *J. Alloys Compd.*, 2011, **509**, 6096–6101, DOI: 10.1016/j.jallcom.2011.03.034.

45 I. Gupta, S. Singh, P. Kumar, S. Bhagwan, V. Tanwar, S. Nehra and D. Singh, Synthetic, structural and optical characteristic of novel color tunable reddish-orange $Gd_4Al_2O_9$: Sm^{3+} nanocrystalline materials for solid-state photonic appliances, *Inorg. Chem. Commun.*, 2023, **148**, 110332, DOI: 10.1016/j.inoche.2022.110332.

46 I. Gupta, D. Singh, S. Singh, P. Kumar, S. Bhagwan and V. Kumar, Structural, optical and Judd-Ofelt analyses of $Gd_{2-x}Eu_xSi_2O_7$ nanocrystals for lighting applications, *Chem. Phys. Lett.*, 2023, **826**, 140670, DOI: 10.1016/j.cplett.2023.140670.

47 Y. Tian, B. Chen, R. Hua, J. Sun, L. Cheng, H. Zhong, X. Li, J. Zhang, Y. Zheng, T. Yu, L. Huang and H. Yu, Optical transition, electron-phonon coupling and fluorescent quenching of $La_2(MoO_4)_3$:Eu^{3+} phosphor, *J. Appl. Phys.*, 2011, **109**, 053511, DOI: 10.1063/1.3551584.

48 J. L. Cheng, H. Tang, X. Yu, Z. Wang, X. Mi and X. Zhang, Synthesis and photoluminescence properties of NUV-excited $NaBi(MoO_4)_2$: Sm^{3+} phosphors for white light emitting diodes, *Opt. Laser Technol.*, 2022, **147**, 107659, DOI: 10.1016/j.optlastec.2021.107659.

49 P. Kumar, D. Singh and I. Gupta, UV excitable $GdSr_2AlO_5$:Eu^{3+} red emitting nanophosphors: structure refinement, photoluminescence, Judd-Ofelt analysis and thermal stability for w-LEDs, *J. Alloys Compd.*, 2023, **966**, 171410, DOI: 10.1016/j.jallcom.2023.171410.

50 M. Luo, X. Sha, B. Chen, X. Zhang, H. Yu, X. Li, J. Zhang, S. Xu, Y. Cao, Y. Wang, X. Wang, Y. Zhang, D. Gao and L. Wang, Optical transition properties, internal quantum efficiencies, and temperature sensing of Er^{3+} doped $BaGd_2O_4$ phosphor with low maximum phonon energy, *J. Am. Ceram. Soc.*, 2022, **105**, 3353–3363, DOI: 10.1111/jace.18299.

51 P. Kumar, D. Singh, I. Gupta and H. Kumar, Synthesis, crystallographic structure, down shifting luminescence of Er(III) activated $GdSr_2AlO_5$ nanophosphors: an efficient green emitter for solid state lighting, *Mater. Sci. Semicond. Process.*, 2023, **167**, 107765, DOI: 10.1016/j.mssp.2023.107765.

52 P. Kumar, D. Singh and I. Gupta, Gadolinium-based Sm^{3+} activated $GdSr_2AlO_5$ nanophosphor: synthesis, crystallographic and opto-electronic analysis for warm wLEDs, *RSC Adv.*, 2023, **13**, 7703–7718, DOI: 10.1039/D3RA00636K.

53 N. Ma, W. Li, B. Devakumar, Z. Zhang and X. Huang, Utilizing energy transfer strategy to produce efficient green

luminescence in $Ca_2LuHf_2Al_3O_{12}$:Ce^{3+}, Tb^{3+} garnet phosphors for high-quality near-UV-pumped warm-white LEDs, *J. Colloid Interface Sci.*, 2021, **601**, 365–377, DOI: 10.1016/j.jcis.2021.05.108.

54 S. Wang, B. Devakumar, Q. Sun, J. Liang, L. Sun and X. Huang, Highly efficient near- UV-excitable $Ca_2YHf_2Al_3O_{12}$:Ce^{3+},Tb^{3+} green-emitting garnet phosphors with potential application in high color rendering warm-white LEDs, *J. Mater. Chem. C*, 2020, **8**, 4408–4420, DOI: 10.1039/D0TC00130A.

55 F. Liao, Y. Zhang and J. Hu, Enhancement of green emission from $Ca_{14}Al_{10}Zn_6O_{35}$:Tb^{3+} phosphors via cross-relaxation energy transfer by Li^+ ions, *J. Lumin.*, 2021, **231**, 117791, DOI: 10.1016/j.jlumin.2020.117791.

56 W. W. Wu, Y. P. Zhang and J. X. Hu, $Ba_3YB_3O_9$ based phosphor ceramic plates with excellent thermal stability for wLED applications, *Dalton Trans.*, 2021, **50**, 5287–5300, DOI: 10.1039/D1DT00194A.

57 H. Tang, D. Yang, H. Li, M. Li and J. Zhu, A narrow-band $RbBaBP_2O_8$:Tb^{3+} green phosphor with high thermal stability for backlighting display application, *J. Lumin.*, 2023, **257**, 119733, DOI: 10.1016/j.jlumin.2023.119733.

58 K. Rawat, A. K. Vishwakarma and K. Jha, Thermally stable $Ca_2Ga_2SiO_7$:Tb^{3+} green emitting phosphor for tricolor w-LEDs application, *Mater. Res. Bull.*, 2020, **124**, 110750, DOI: 10.1016/j.materresbull.2019.110750.

59 F. Chi, L. Pan, B. Jiang, Z. Ji, J. Cheng, B. Wang and S. Liu, Luminescence properties of multicolor emitting La_4GeO_8:Tb^{3+}, Eu^{3+} phosphors, *Ceram. Int.*, 2023, **49**, 2522–2530, DOI: 10.1016/j.ceramint.2022.09.230.

60 Y. K. Zheng, T. S. Yang, Y. F. Xiang, K. Xiong, D. Yang, Z. Y. Fang, S. Q. Yang and J. Zhu, $Ba_3(ZnB_5O_{10})PO_4$:Tb^{3+} green phosphor: microwave-assisted sintering synthesis and thermally stable photoluminescence, *J. Alloys Compd.*, 2022, **911**, 165087, DOI: 10.1016/j.jallcom.2022.165087.

61 J. L. Song, H. Li, Y. F. Xiang and J. Zhu, Content and temperature quenching of Tb^{3+}- activated Bi_3TeBO_9 green phosphor excited by NUV/VIS light, *J. Solid State Chem.*, 2022, **313**, 123317, DOI: 10.1016/j.jssc.2022.123317.

62 J. F. Yang, H. Y. Wu, L. N. Song, X. X. Wang, J. C. Dong, S. C. Gan and L. C. Zou, A novel synthesis route to monodisperse $Na_5Lu_9F_{32}$:Tb^{3+} phosphors with superior thermal stability, *J. Lumin.*, 2018, **204**, 533–538, DOI: 10.1016/j.jlumin.2018.08.061.

63 S. Limbu, L. R. Singh and G. S. Okram, The effect of lithium on structural and luminescence performance of tunable light-emitting nanophosphors for white LEDs, *RSC Adv.*, 2020, **10**, 35619–35635, DOI: 10.1039/D0RA05433J.

64 P. Kumar, D. Singh and H. Kumar, Gel-combustion synthesis, structural and optoelectronic analyses of Tb^{3+} activated $LaSr_2AlO_5$ nanophosphors: a green emitter for displays, *Mater. Sci. Semicond. Process.*, 2024, **174**, 108162, DOI: 10.1016/j.mssp.2024.108162.

65 I. Gupta, D. Singh, S. Singh, P. Kumar, S. Bhagwan and V. Kumar, Structural and photophysical measurements of Er^{3+} doped $Gd_4Al_2O_9$ nanophosphors for NUV excitable solid-state lighting applications, *Chem. Phys. Lett.*, 2023, **814**, 140350, DOI: 10.1016/j.cplett.2023.140350.

66 P. Kumar, S. Singh, I. Gupta, K. Nehra, V. Kumar and D. Singh, Structural and luminescent behaviour of Dy(III) activated $Gd_3Al_5O_{12}$ nanophosphors for white-LEDs applications, *Mater. Chem. Phys.*, 2023, **295**, 127035, DOI: 10.1016/j.matchemphys.2022.127035.

67 B. Deng, Y. Yang, W. Chen, X. Xie, R. Yang, C. Li and R. Yu, Synthesis and characterization of thermostable Dy^{3+}-doped $La_5NbMo_2O_{16}$ yellow-emitting phosphors for w-LEDs, *J. Mater. Sci.: Mater. Electron.*, 2022, **33**, 23042–23053, DOI: 10.1007/s10854-022-09071-2.